TU Delft

Delft University of Technology

Document Version
Final published version

Licence
CC BY

Citation (APA)
Guis, R. H., Arabul, M. U., Zhou, Z., & Verbiest, G. J. (2026). Atomic force microscope cantilever as focused GHz ultrasound transducer. *Journal of Sound and Vibration*, *644*, Article 120034. https://doi.org/10.1016/j.jsv.2026.120034

Important note
To cite this publication, please use the final published version (if applicable).
Please check the document version above.

Copyright
In case the licence states “Dutch Copyright Act (Article 25fa)”, this publication was made available Green Open Access via the TU Delft Institutional Repository pursuant to Dutch Copyright Act (Article 25fa, the Taverne amendment). This provision does not affect copyright ownership.
Unless copyright is transferred by contract or statute, it remains with the copyright holder.

Sharing and reuse
Other than for strictly personal use, it is not permitted to download, forward or distribute the text or part of it, without the consent of the author(s) and/or copyright holder(s), unless the work is under an open content license such as Creative Commons.

Takedown policy
Please contact us and provide details if you believe this document breaches copyrights.
We will remove access to the work immediately and investigate your claim.

This work is downloaded from Delft University of Technology.

Journal of Sound and Vibration 644 (2026) 120034

Contents lists available at ScienceDirect

Journal of Sound and Vibration

journal homepage: www.elsevier.com/locate/jsvi

Atomic force microscope cantilever as focused GHz ultrasound transducer

R.H. Guis [a], M.U. Arabul [b], Z. Zhou [b], G.J. Verbiest [a,*]

[a] Faculty of Mechanical Engineering, Department of Precision and Microsystems Engineering, Delft University of Technology, 2628 CD, Delft, The Netherlands
[b] ASML Netherlands b.v., 5504DR, Veldhoven, The Netherlands

ARTICLE INFO

Keywords:
Atomic force microscopy
Picosecond ultrasonics
Photo-acoustics
Elastic wave propagation
Acoustic focusing
Mode conversion
Acoustic transducer

ABSTRACT

We demonstrate that an atomic force microscope (AFM) tip acts as a nano-acoustic horn, focusing GHz ultrasound into its apex through gradual impedance matching. Using photo-acoustic pump–probe measurements, we show tip echoes exceeding geometric expectations by up to 150× between 20–50 GHz. Mode conversion near the apex reduces longitudinal signal strength, but optimizing tip geometry can suppress this effect and enhance transmission efficiency. These results establish AFM cantilevers as effective GHz ultrasound transducers, enabling nanometer-scale acoustic focusing and paving the way for high-resolution subsurface acoustic atomic force microscopy.

1. Introduction

Acoustic microscopy is well-known for its intrinsic ability to penetrate opaque materials and provide three-dimensional (3D) structural information, capabilities well demonstrated at the macroscale in medical ultrasound and industrial non-destructive testing [1]. These advantages carry over conceptually to the nanoscale, where acoustic waves could, in principle, reveal subsurface features inaccessible to light or electrons. However, despite these promising characteristics, practical acoustic imaging techniques at the nanoscale have not yet been realized [2].

To realize acoustic imaging techniques at the nanoscale, the ultrasound wavelength must also be in the nanometer range due to the diffraction limit [3]. Therefore, one needs ultrasound frequencies around 100 GHz to be able to apply conventional pulse-echo based ultrasound methods. Moreover, the obtainable spatial resolution, which should also be in the nanometer range, is limited by the size of the ultrasound transducer. Partial solutions for these requirements exist; (i) integrating ultrasound transducers into atomic force microscopes has enabled MHz up to low GHz ultrasound imaging with nanometer spatial resolution set by the tip size [4–6], but without the required temporal resolution resulting in a loss of depth resolution, and (ii) ultrasound frequencies around 100 GHz are possible via photo-acoustic generation using femtosecond laser pulses [7], but here the transducer size-and thus spatial resolution-is ultimately limited by the optical diffraction limit of the excitation wavelength.

Recent developments in photo-acoustics, in particular, the introduction of asynchronous optical sampling [8,9], enabled the fast generation and detection of acoustic waves with frequencies up to tens to hundreds of GHz, theoretically, within milliseconds. In combination with the high ultrasound frequencies, this would in principle allow for extending AFM-based acoustic imaging to the GHz regime (10–100 GHz), if the AFM cantilever itself can be used as an acoustic transducer.

* Corresponding author.
E-mail address: g.j.verbiest@tudelft.nl (G.J. Verbiest).

https://doi.org/10.1016/j.jsv.2026.120034
Received 16 December 2025; Received in revised form 10 July 2026; Accepted 28 July 2026
Available online 5 August 2026
0022-460X/© 2026 The Author(s). Published by Elsevier Ltd. This is an open access article under the CC BY license (http://creativecommons.org/licenses/by/4.0/).

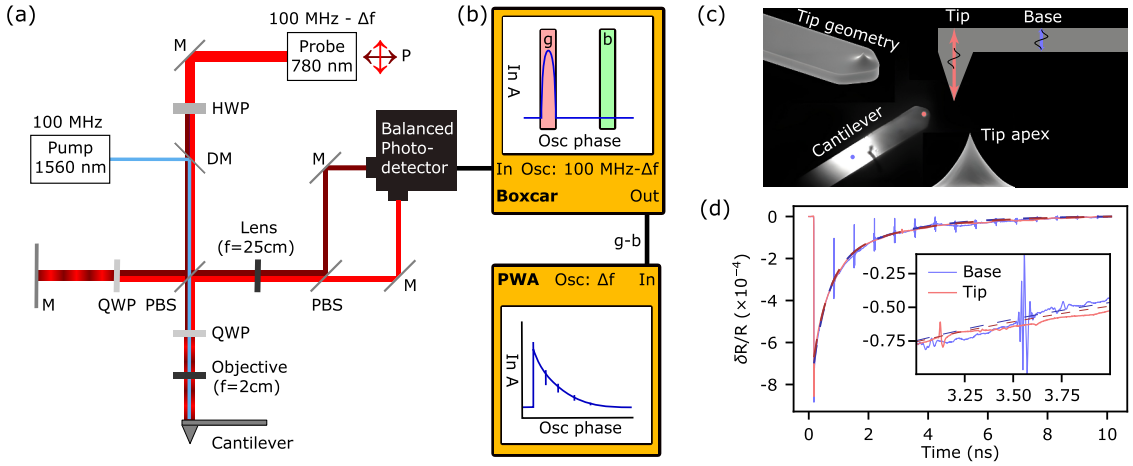


Fig. 1. Experimental setup: (**a**) Schematic of the optical setup: a pump pulse excites acoustic waves in a cantilever; probe reflection changes are measured against a reference using a balanced photodetector. Optical components: Dichroic Mirror (DM), Half Wave Plate (HWP), Polarized Beam Splitter (PBS), Mirror (M), and Quarter Wave Plate (QWP). (**b**) A boxcar extracts pulse amplitudes g with respect to background b, and PWA reconstructs the signal using the pump-probe offset frequency. (**c**) Optical image of the cantilever with tip (red) and base (blue) measurement points, alongside SEM images of a similar Scout70 tip provided by the manufacturer [14]. (**d**) Acoustic signals at the base (blue) and tip (red), showing an initial thermal rise, slow decay, and distinct acoustic echoes. An inset highlights the tip echo (3.1 ns); exponential fits (black) are used to remove thermal background. (For interpretation of the references to color in this figure legend, the reader is referred to the web version of this article.)

Therefore, it is crucial to study and understand the propagation of GHz acoustic waves through the tip of an AFM cantilever. Simulations in pyramidal AFM tips show that such waves do propagate through AFM cantilevers [10], but little of the acoustic power reaches the actual tip apex. These simulations were experimentally verified in millimeter scale models of AFM cantilevers [11] and at GHz frequencies in actual AFM cantilevers with truncated tips [12]. Recent work showed that, even without truncating the AFM tip, it is possible to resolve the GHz acoustic echo from [13] in the time domain. Although not quantified in the paper, the observed loss of power between ultrasound excitation and ultrasound reflection was surprisingly much less than the relative area of the photo-acoustic excitation and the AFM tip apex, leaving open questions about the exact GHz ultrasound propagation in AFM tips. An even lower decrease in tip echo amplitude is simulated in the same work, where acoustic mode conversions are also predicted but not experimentally found.

Here we show that the tip of an AFM cantilever acts as an acoustic horn, naturally focusing the incoming GHz ultrasound at its base to its apex. We experimentally quantify the focusing factor FF Eq. (5), which is the detected amplitude of the acoustic echo in the tip over the expected amplitude. We base the expected amplitude on the geometric loss, assuming the acoustic energy travels down as a plane wave, from the ratio of the optical excitation area and tip apex areas, as well as the acoustic attenuation extrapolated for the sound's propagation through the length of the tip. We analyze this focusing gain as a function of frequency and find that the gain decreases from 150 to 50 when the frequency increases from 20 GHz to 50 GHz. We also observe that mode conversion near the tip apex, which transfers energy between longitudinal and transversal waves. By using acoustic horn theory, we show that the geometry of the commercial AFM cantilever tip is not optimal but has a focusing in line with the experimental observations. Engineering the geometry of the AFM tip can further optimize GHz acoustic transmission, enabling to focus sound on a nanometer-scale spot on a sample when in contact.

2. Photo-acoustic setup

We use a photo-acoustic setup to measure GHz ultrasound propagation through an AFM tip (Fig. 1). A pulsed 1560 nm pump laser (≤100 fs) generates acoustic waves by illuminating the back of an AFM cantilever, while a synchronized 780 nm probe laser (≤100 fs) detects the resulting variations in cantilever reflectivity. The pump operates at 100 MHz and the probe at 100 MHz–Δf, enabling asynchronous optical sampling [8].

Both beams are combined via a dichroic mirror. The pump passes through polarization optics and is focused on the cantilever, launching acoustic waves. The probe beam is split into a reference and measurement arm using a half-wave plate (HWP) and a polarizing beam splitter (PBS). In the reference arm, light reflects off a mirror via a quarter-wave plate (QWP) and re-enters the PBS. In the measurement arm, light reflects off the cantilever surface, where acoustic waves modulate reflectivity via refractive index changes [15] and beam divergence [16].

The recombined probe beams enter a balanced photodetector (Femto HBPR-200M-30K-SI-FST [17]), which detects small reflectivity changes. A lens ensures beam overlap, and polarization is adjusted via the HWP. As Fig. 1b shows, the electrical signal is processed by a Zurich Instruments UHFLI-600MHz lock-in amplifier [18], where a boxcar extracts the peak (g) and background (b) of each probe pulse , using 60 ° boxcar windows on a reference locked to the probe repetition rate (f_{probe} = 100 MHz–Δf). The

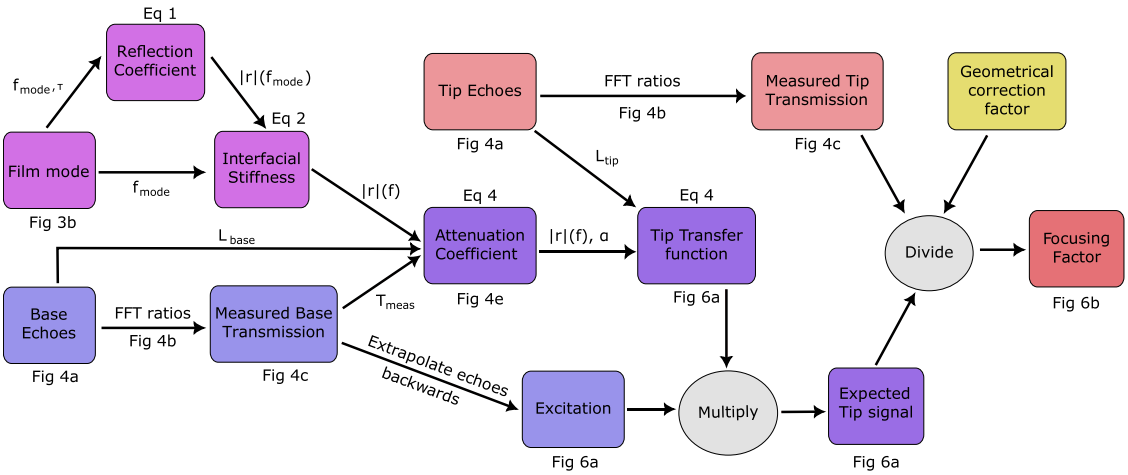


Fig. 2. Block diagram describing the analysis. From the measured film mode in Fig. 3, we extract the mode frequency and decay time constant. Via the reflection coefficient at the film frequency (Eq. (1)), we calculate the interfacial stiffness of the Al-Si interface. By taking the ratio between the echoes in the Si base from Fig. 4, we determine the frequency-dependent transmission factor of each acoustic round trip. Combined with the base thickness extracted from the time of flight, and the frequency-dependent reflection coefficient extracted from the interfacial stiffness found from the film mode, we use Eq. (2) to find the frequency-dependent attenuation of the Si beam. We use the time-of-flight extracted from the tip echoes to extrapolate the attenuation over the length of the tip with Eq. (4). This gives us the transfer function for the tip, which we multiply by the excitation found from dividing the first base echo by the base echo ratio to find the expected signal for a sample with a thickness equal to the length of the tip. We compare this to the actually measured echo spectrum on the tip, where we add a geometric correction factor to compensate for the loss in area between the excitation spot and the tip apex. This focusing factor is calculated using Eq. (5).

variation of probe pulse intensity signal $g - b$ is analyzed as a function of time (delay between pump and probe laser) using a periodic waveform analyzer (PWA) with the boxcar as input and locked to the offset frequency Δf and using $1/\Delta f$ as the time base. The analyzed signals contain 1000 averages.

Measurements were done on NuNano Scout70 cantilevers [14], with locations indicated in Fig. 1c. SEM and optical images show base (blue) and tip (red) measurement points. Despite the small tip radius (5 nm) compared to the excitation spot (radius 2.5 μm), measured echoes (Fig. 1d) are much stronger than expected from the energy scaling, suggesting acoustic focusing due to the horn-like geometry of the cantilever, as we will show in the rest of this paper.

3. Results

We experimentally demonstrate efficient GHz acoustic wave focusing through an AFM tip. First, we analyze the aluminum thin film transducer and then the heat transport arising from the pulsed pump laser in the AFM cantilever through the Al/Si interface. Second, we analyze multiple round trips in the cantilever base to quantify propagation and Al/Si interface losses. This is followed by a detailed analysis of the echoes from the AFM cantilever tip. Then, as AFM probes are typically manufactured from a single piece of monocrystalline silicon [19,20], consistent with the same resistivity values specified in the cantilever and in the tip for the Scout70 cantilevers used [14], we extrapolate the acoustic transmission through the Si base over a distance equal to twice the length of the tip and estimate the expected transmission based on the surface area's of the excitation and the tip apex. Comparing the expected and measured tip transmissions shows a 50× larger tip echo than expected. In this analysis, we exclude local resonance effects, as the acoustic frequencies of the order of 10–100 GHz correspond to wavelengths of 80-800nm in silicon, which are more than 3 orders of magnitude smaller than the tip height or the diameter of the tip's base. A flow chart of how we determine the focusing factor is shown in Fig. 2. Finally, we provide a theoretical validation of the observed amplification.

3.1. Aluminum thin film transducer

To characterize the thin aluminum film and its bonding to the silicon cantilever, we analyze high-frequency acoustic oscillations that appear immediately after laser excitation (Fig. 3a and b). These oscillations form a damped standing wave rather than distinct echoes, because the thickness of the film is comparable to the acoustic wavelength. By fitting a damped sine function, we extract the frequency and decay rate of the second bound acoustic mode, which is expected because the acoustic impedance of Si is larger than that of Al. From the measured mode frequencies f_m (116 GHz at the base, 112 GHz at the tip), we determine the thicknesses of Al films through $d = \frac{(2n+1)}{4} v_{\mathrm{Al}}/f_m$ with $n = 1$ (second bound mode) and the speed of sound in Aluminum $v_{\mathrm{Al}} = 6420$ m/s to be 41.5 nm and 43.0 nm, in the base and tip locations, respectively, closely matching the nominal 40 nm value given by the manufacturer [14]. The fundamental bound mode (n = 0) around 40 GHz is also observed in the echo spectrum (see Fig. 4b) and in the excitation (see Fig. 6a), but it appears broader and weaker. This can be attributed to the non-ideal interface between the Al and Si, which acts as a low-pass filter and confines the second bound mode more effectively within the film (Eq. (2)).

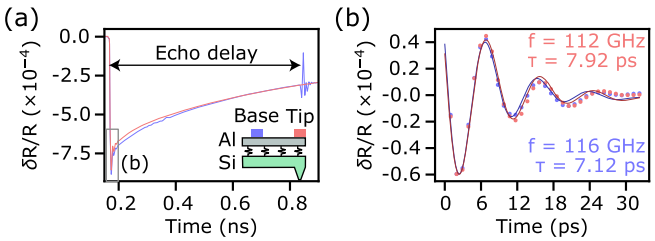


Fig. 3. (**a**) Schematic side view of the cantilever illustrating the measurement position on the base (blue) and tip (red). Zooming into the signal up to 1 ns reveals a distinct acoustic signal in the aluminum film, as shown in (**b**). (**b**) Zoom in on the signal in the aluminum film with in continuous lines the fits to a damped harmonic oscillator, from which we extract the main frequency f and decay time τ. (For interpretation of the references to color in this figure legend, the reader is referred to the web version of this article.)

We extract the interfacial stiffness k between aluminum and silicon from the amplitude decay of the acoustic mode [21]. Assuming that the attenuation in the Al film itself is much smaller than the wave transmission through the Al/Si-interface, we use the measured decay times of $\tau = 7.12$ ps at the base and $\tau = 7.92$ ps at the tip to determine the reflection coefficients of $|r| = 0.16$ (base) and $|r| = 0.19$ (tip) at the film mode frequency using Eq. (1). These are significantly higher than the ideal value of 0.058 based on acoustic impedance mismatch.

$$|r|(f_m) = \exp\left(\frac{-2d}{\tau v_{\mathrm{al}}}\right) \tag{1}$$

By assuming an imperfect bond between the Al film and the underlying Si, following Lee et al. [21], we find interfacial stiffness values of 4.43×10^{19} N/m^3 (base) and 3.51×10^{19} N/m^3 (tip) from Eq. (2). As the attenuation in the Al film would reduce the measured reflection $|r|$ even more, the values found of $|r|$ represent a lower bound and the values of k represent an upper bound.

Using the interfacial stiffness values found, the frequency-dependent reflection coefficients can be calculated using:

$$r = \frac{Z_{\mathrm{Al}} - Z_{\mathrm{Si}} + \frac{i2\pi f Z_{\mathrm{Al}} Z_{\mathrm{Si}}}{k}}{Z_{\mathrm{Al}} + Z_{\mathrm{Si}} + \frac{i2\pi f Z_{\mathrm{Al}} Z_{\mathrm{Si}}}{k}}, \tag{2}$$

where $Z_{Al} = 17.28$ MRayl and $Z_{Si} = 19.7$ MRayl are the acoustic impedance of Aluminum and Silicon, respectively. We will later use Eq. (2) to compute the lower bound of r for acoustic waves that cross the Al/Si interface.

3.2. Thermal transport through Al/Si interface

To isolate the acoustic signal from the thermal background in Fig. 1d, we fit a double exponential to the thermal decay. The extracted time constants are $\tau_1 = 0.47$ ns, $\tau_2 = 2.28$ ns (base) and $\tau_1 = 0.53$ ns, $\tau_2 = 2.63$ ns (tip).

In picosecond ultrasonics, heat transfer is typically described by the two-temperature model [22], with fs-ps electron-phonon coupling. However, the slower (ns) timescales observed point to a different mechanism: heat diffusion through the Al film to the Al–Si interface. Although Al and Si have similar thermal diffusivities (97 and 88 m^2/s), the interface acts as a thermal Kapitza resistance, probably arising from the heat transport being governed by electrons in Al and by phonons in Si. This results in the observed, much slower decay component [23].

From theory, we know that Kapitza conductivity can be estimated through

$$\sigma_K = \rho C d/\tau, \tag{3}$$

where $\rho = 2.7$ g/cm^3, $C = 900$ J/kg K and d are the aluminum film's density, specific heat, and thickness. Using the found Al film thicknesses, we find $\sigma_K = 3.88 \times 10^7$ Wm^{-2}K^{-1}, about 10× lower than literature values [24]. This discrepancy likely arises from interface roughness or imperfections [25], which hinder thermal coupling across the boundary. This is supported by the interfacial stiffness k of the Al/Si interface measured in this sample, which is low compared to an ideal Al-Si interface.

3.3. Attenuation by silicon and Al/Si interface

After subtracting the thermal background, we apply a 5 GHz high-pass filter to isolate the acoustic signal (Fig. 4a and b). At the cantilever base, periodic echoes are observed with an average time-of-flight of 0.676 ns, corresponding to a beam thickness of 2.80 μm when using a speed of sound c_L of 8430 m/s for silicon. This thickness is consistent with the manufacturer's specifications [14].

The spectra of each of the echoes are shown in Fig. 4b. By taking the ratio between consecutive echoes (Fig. 4c), we obtain a frequency-dependent amplitude loss, overlapping for all shown echo pairs. This is related to the measured transmission $T_{\mathrm{meas}} = |t|^2$ through the Al–Si interface and the Si base, where t is the complex acoustic transmission coefficient of the interface. Ignoring attenuation during propagation, the reflection coefficient is estimated as $|r|_{\mathrm{upper}} = \sqrt{(1-|t|^2)^2} = \sqrt{(1-T_{\mathrm{meas}})^2}$, as the acoustic wave

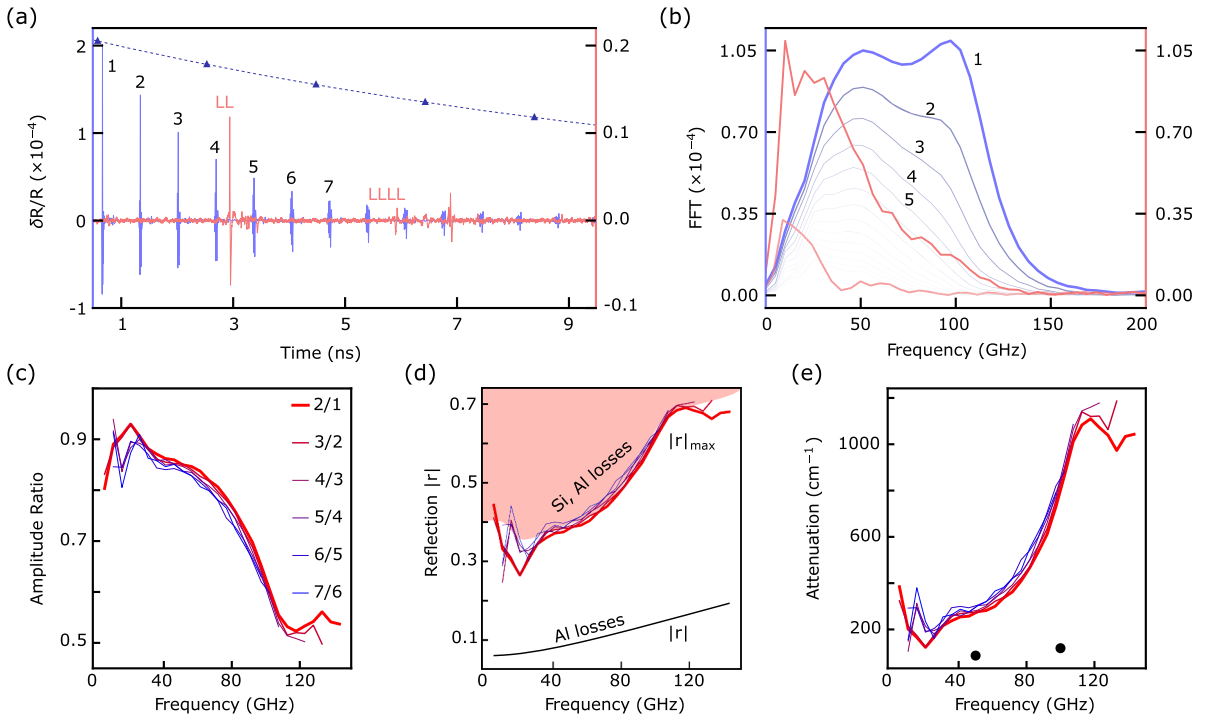


Fig. 4. (**a**) Acoustic signalsat the base (blue) and tip (red) after removing the thermal contribution shows distinct acoustic echoes. The dashed line indicates the expected attenuation during propagation in the silicon base from literature [26]. (**b**) FFT of a 200 ps time window around the first echo in the base (blue) and the tip (red). The main frequency in the base echo is 50 GHz and in the tip 25 GHz. The shift towards lower frequencies for the tip echo is due to a combination of frequency-dependent attenuation and focusing by the tip.(**c**). Ratio between consecutive echoes. The detected amplitude ratio falls off with frequency. (**d**). Lower and upper limits for reflection coefficient as a function of frequency, estimated from the film mode, and back reflections respectively. (**e**). Estimated frequency-dependent attenuation coefficient when attributing all losses to the silicon. The estimated values are much higher than the ones at 50 GHz and 100 GHz from literature [26], indicated with black dots. The peak at ~ 116 GHz corresponds to the aluminum-film mode resonance. (For interpretation of the references to color in this figure legend, the reader is referred to the web version of this article.)

passes twice through the Al/Si interface. This provides an upper bound for $|r|$, as the attenuation in the Al film or Si base contributes to the observed T_{meas} as well, and thus neglecting it in the analysis overestimates $|r|$.

The obtained upper bound $|r|_{\text{upper}}$ indeed exceeds the lower bound that we compute from the film mode using Eq. (2) and the extracted interfacial stiffness for the base (Fig. 4d). The difference between these two bounds is the inclusion of acoustic losses in the silicon base and/or aluminum film. By assuming negligible losses in the Al film which is orders of magnitude thinner than the Si cantilever base, the difference between the lower and upper bound purely originates from attenuation α in the silicon. Hence, the measured signal from the backside of the cantilever T_{meas}, after transmission through the interface twice, determining the upper bound, is given by:

$$T_{\text{meas}} = (1 - |r|^2)\mathrm{e}^{-2\alpha L}, \tag{4}$$

where L is the thickness of the silicon base and $|r|$ is the lower bound. By solving this equation for α (Fig. 4e), we find that α exceeds the reported intrinsic losses in silicon at 50–100 GHz [26]. Moreover, we observe a prominent peak at 116 GHz due to the second bound mode in the aluminum film, which absorbs energy and thereby effectively increases loss.

3.4. Echoes and mode conversions in the AFM tip

Let us now focus on the acoustic echoes from the tip apex shown in red in Fig. 4a. These echoes are separated by a time delay of 2.96 ns, corresponding to a tip height (including base) of 12.47 μm when using $c_L = 8430$ m/s. This tip height is well within the range of 10–13 μm specified by the AFM cantilever manufacturer [14]. By time-shifting both tip echoes relatively by their time of flight, overlaying them in Fig. 5a, we observe more additional oscillations in $\delta R/R$ than just from the echo. We attribute these to acoustic mode conversions at the cantilever tip, as predicted by Delalande et al. [13]. At sharp geometric transitions, longitudinal (L) waves partially convert into transverse (T) waves, a phenomenon also observed in graphene [27]. Due to the different velocity of T waves compared to L waves ($c_T = 5840$ m/s vs. $c_L = 8430$ m/s in silicon [28]), these converted waves generate additional peaks in $\delta R/R$ measurements with distinct arrival times.

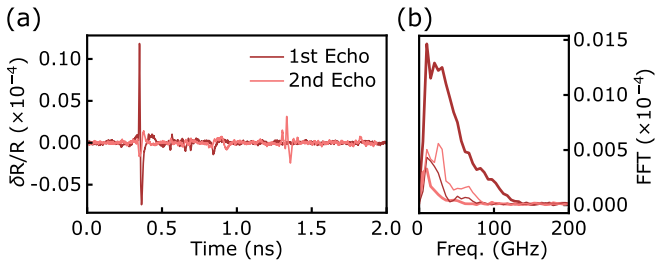


Fig. 5. (**a**). Zoom on the echoes from the tip apex. The longitudinal wave after two round-trips through the tip (LLLL) is time-shifted by the time-of-flight between excitation and first LL echo. Longitudinal (LL) and converted into slower transversal (LT) reflections from the tip apex. Because the detection method is more sensitive to longitudinal waves, the LTTL-peak appears larger than the LT-peak from the first echo. (**b**). FFT around echoes in panel (**a**) shows that the frequency content is very similar for the L and T mode echoes.

We label each signal by its propagation and conversion path. For example, an LT signal corresponds to a longitudinal wave traveling down the tip, converting to a transverse wave at the apex, and returning. Given a measured tip height of 12.47 μm, the expected LT delay relative to the LL peak is 0.67 ns; experimentally, a peak appears at 0.55 ns, within 20% of the estimate, likely due to variation in elastic moduli with crystal orientation and doping [28]. The average shear speed of sound through the horn to explain this time of flight is $6143\ m/s$, with a corresponding effective stiffness of $86.1\ GPa$. This measured effective stiffness slightly exceeds the commonly quoted bulk transverse-wave stiffness in silicon of 79.6 GPa [28]. Given the elastic anisotropy of single-crystal silicon and the presence of guided modes in the horn structure, such deviations are plausible [29]. A larger LTTL peak, arriving 1 ns after the second LL echo, matches the expected second-order LT path. As this returns as a longitudinal wave, it generates stronger surface displacement and therefore in a larger signal, as the setup is more sensitive to out-of-plane deformations [16,30]. Fig. 5b confirms that mode conversion spans a wide frequency range. The weaker LLLT and LTTT echoes (at 0.5 ns and 1.5 ns) arrive as transverse waves, resulting in low amplitudes. Notably, the LTTL peak is roughly twice as large as the LLLL echo, indicating substantial mode conversion. Tailoring the tip geometry could suppress this and improve L-wave transmission to the tip apex. The mode conversion is believed to originate from the strong spatial gradient of the tip boundary at the tip apex, which promotes coupling between longitudinal and transverse displacement components [31,32]. Although weaker conversion may also occur along other parts of the tip boundary, the elastic energy is concentrated near the apex, making the corresponding converted signal dominant in the measurements.

3.5. Acoustic focusing by the cantilever tip

While the arrival time of the tip echoes is as expected, the echo amplitude is surprisingly high-far exceeding the 500× amplitude reduction predicted from the ratio of the optical excitation radius to the tip radius. The key point is that we measure the acoustic amplitude in the Al film, not acoustic energy. Energy depends on amplitude squared (and scales with the area of the wave), but our signal only depends on the amplitude itself. This means that the geometric loss we see is not set by the area ratio, but simply by the ratio of the excitation radius and the tip radius.

When considering only the amplitude in the time domain, which ignores the longer pathlength and therefore stronger attenuation in the tip, the detected amplitude is only 20 times weaker than Fig. 4a), already resulting in a focusing factor of 25.

Extrapolating the attenuation over the length of the tip, we calculate a frequency-dependent focusing factor. Assuming a straight-tip model and thus neglecting cone geometry, we estimate the expected echo amplitude $T_{\mathrm{tip}_{\mathrm{expected}}}(f)$ using Eq. (4), combining interface and propagation losses derived from base measurements, and setting $L = 12.47$ μm. The excitation $S_{\mathrm{Exc}}(f)$ is estimated by dividing the first base echo spectrum by the amplitude decay between consecutive echoes (red line in Fig. 6a). Multiplying this excitation by the calculated tip transmission yields the expected tip echo, which is compared to the measured signal in Fig. 6a.

$$FF(f) = \frac{r_{\mathrm{laserspot}}}{r_{\mathrm{tip}}} \frac{S_{\mathrm{tip}}(f)}{S_{\mathrm{Exc}}(f) \cdot T_{\mathrm{tip}_{\mathrm{expected}}}(f)} \tag{5}$$

To obtain the focusing factor FF (Eq. (5)) shown in Fig. 6b, we compute the measured-to-estimated spectrum ratio and multiply it by 500 (the geometric loss factor). Above 40 GHz, this gain is roughly constant and equal to 50. Below 40 GHz, the gain increases up to 150 at 15 GHz. This frequency-dependent gain is also reflected in the frequency spectrum of all the acoustic echoes shown in Fig. 4b. The echoes from the tip carry much more energy at lower frequencies than the echoes in the cantilever base. The AFM tip thus functions as an acoustic horn [33], concentrating energy into the tip and enhancing return signal strength. Optimizing the tip geometry for a specific frequency range could further improve transmission efficiency.

Although the focusing factor was only determined for a single representative tip geometry to demonstrate that the AFM tip can guide GHz acoustic waves toward the apex, we observe qualitatively similar behavior across multiple probes. In particular, detectable tip echoes are also observed for AFM probes with substantially different geometries, such as pyramid-shaped tips (NanoAndMore, CONTR), as shown in Fig. 7. This indicates that the acoustic guiding effect is robust to variations in tip geometry. A detailed quantitative comparison between different tip shapes is beyond the scope of the present work.

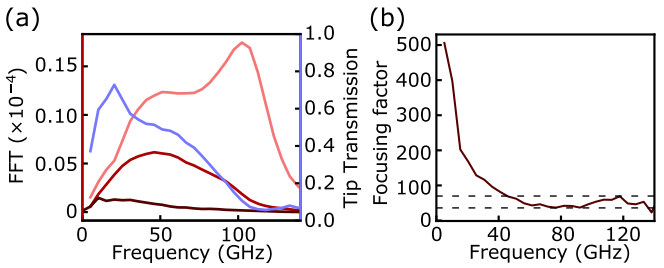


Fig. 6. (**a**). The acoustic excitation (red) is estimated by dividing the FFT of the first base echo by the base transmission ratio (see Fig. 4b, c). Multiplying this with the expected transmission through the full height of the cantilever tip (blue), estimated from Eq. (4), we find the estimated spectrum of the first tip (medium red). To find the focusing factor, panel (**b**), we divide the estimated spectrum (medium red) with the detected first echo from the tip (dark red) and multiply with 500 to compensate for the geometrical loss factor. (For interpretation of the references to color in this figure legend, the reader is referred to the web version of this article.)

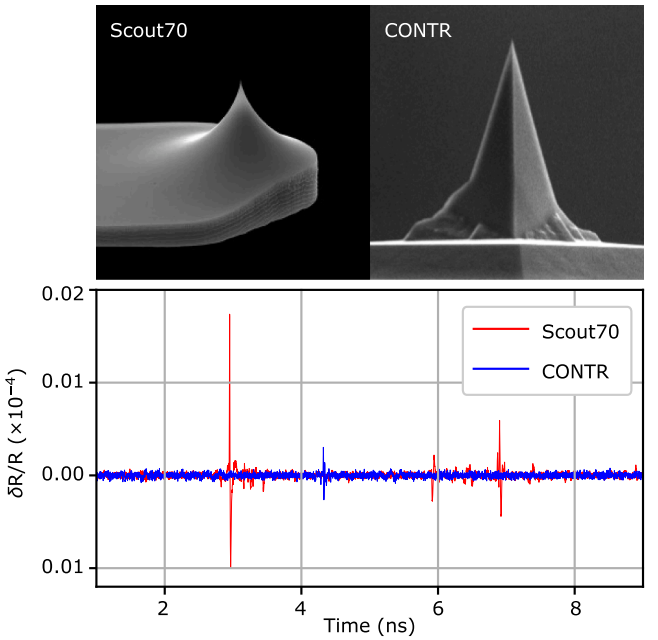


Fig. 7. Representative SEM images from the manufacturers illustrating the nominal conical and pyramidal geometries of AFM probes used, and the acoustic reflections from a conical 12 μm AFM tip (Scout70), and a 18 μm pyramid shaped NanoAndMore CONTR AFM probe.

3.6. Theoretical validation of AFM tip acoustics

The observed transmission through the AFM tip significantly exceeds predictions based on the ratio of excitation and tip surface areas. This discrepancy arises because the tip geometry features a gradual taper, rather than an abrupt transition. Such a taper enables acoustic impedance matching along the propagation path, reducing reflections and enhancing transmission [34]. Similar behavior is well known in tapered RF transmission lines [35] and optical fibers [36].

The local acoustic impedance along the tip is given by:

$$Z(z) = \frac{\rho c}{A(z)}, \tag{6}$$

where $A(z)$ is the cross-sectional area at position z, and ρ, c are the material's density and speed of sound.

To estimate the reflection from a continuously tapered tip, we use the approximation from transmission line theory [37]:

$$\Gamma(\lambda, L) = \frac{1}{2}\int_0^L e^{-2i\frac{2\pi}{\lambda}z}\frac{d}{dz}\left[\ln\left(\frac{Z(z)}{Z_0}\right)\right]dz, \tag{7}$$

where λ is the acoustic wavelength, L is the tip length, and Z_0 is the impedance at the tip base. This approach assumes negligible reflections from the tip boundaries (except the apex) [37]. We use this theory to estimate which tip geometries achieve good focusing and high transmission.

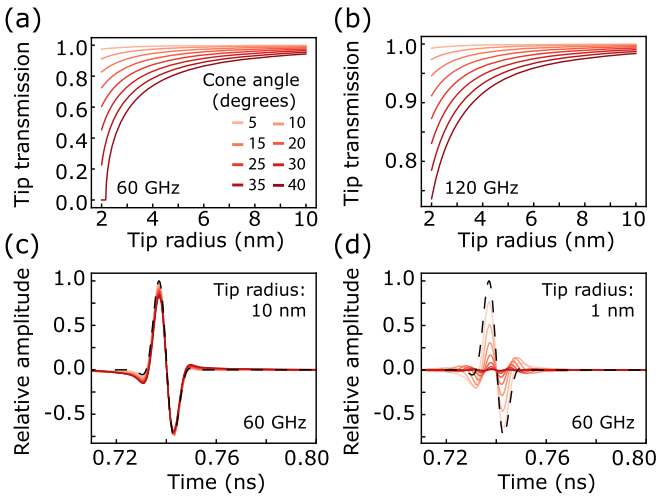


Fig. 8. Calculated acoustic transmission through a 3 μm long conical horn with different cone angles and tip radii. Transmission for (**a**) 60 GHz and (**b**) 120 GHz acoustic wave for different cone angles. Relative amplitude (compared to excitation in black) for acoustic pulses with a center frequency of 60 GHz with a tip radius of (**a**) 10 nm and (**b**) 1 nm.

The manufacturer specified the probe used in the experiment to have a cone angle between 15 and 45 degrees (nominal 25 degrees) over the last μm of the tip and a tip radius less than 10 nm (nominal 5 nm) [14]. Using this model, we simulate transmission through linear conical horns in silicon at 60 GHz and 120 GHz, varying cone angle and tip radius in this range while keeping horn length constant (Fig. 8a and b). Results show that steeper tapers and larger tip radii reduce initial impedance mismatch and improve transmission. Higher frequencies are better guided through the horn, though attenuation, excluded in this model, is stronger at these frequencies.

To model pulsed excitation, we compute the Fourier spectrum of a 60 GHz-centered pulse. For each frequency component, we calculate the transmission and apply the phase shift $\phi(f) = 4\pi f L/c$ over the roundtrip length. Multiplying the spectrum by the transmission response and applying the inverse Fourier transform yields the time-domain result shown in Fig. 8c and d.

While these simulations do not include mode conversion, which is prominent in measurements (Fig. 5), they predict near-unity transmission for realistic tip geometries (e.g., 10 nm tip radius at 60 GHz) supporting that such geometries could indeed be used to focus GHz acoustic waves. Finite element simulations that include mode conversion confirm this trend: Delalande et al. [13] report LL echo amplitudes exceeding one-third of the excitation amplitude. Their simulated waveform closely matches our measured signal, underscoring that optimizing tip geometry can significantly enhance acoustic focusing performance.

As the relative impedance change is largest near the tip apex, we expect that the tip radius and cone angle near the tip are the most important parameters for acoustics focusing. Their exact influence should be investigated in more detail in further studies.

4. Conclusion

We showed that the AFM tip geometry effectively focuses GHz acoustic waves into the tip apex, acting as a nano-acoustic horn. Base measurements reveal that high-frequency losses are dominated by excitation of the aluminum film's bulk mode. Thermal treatment could improve the interface and reduce these losses, thereby enhancing high-frequency transmission and improving imaging resolution.

Comparing the estimated tip transmission (based on interface and propagation losses) to the measured echo yields an amplitude gain of 50–150× between 20–50 GHz. However, significant mode conversion occurs at the tip: the LTTL peak is twice as strong as the LLLL mode, indicating energy loss to transverse waves, which are poorly detected.

Optimizing tip geometry could be used to suppress mode conversion and target specific frequencies. We only investigated a conical tip geometry and only varied cone angle and tip diameter. Other tip geometries, such as an exponential horn, may perform even better. Note that the tip geometry optimization should consider the attenuation within the horn, as it limits the maximum tip length. Ultimately, tip geometry optimization can enhance longitudinal wave transmission and reduce averaging time in high-resolution photo-acoustic subsurface atomic force microscopy imaging.

CRediT authorship contribution statement

R.H. Guis: Writing – review & editing, Writing – original draft, Visualization, Validation, Software, Resources, Methodology, Investigation, Formal analysis, Data curation, Conceptualization; **M.U. Arabul:** Writing – review & editing, Supervision, Project administration; **Z. Zhou:** Writing – review & editing, Supervision, Project administration, Funding acquisition; **G.J. Verbiest:** Writing – review & editing, Writing – original draft, Supervision, Resources, Project administration, Funding acquisition, Conceptualization.

Declaration of competing interest

The authors declare the following financial interests/personal relationships which may be considered as potential competing interests:

G. J. Verbiest reports financial support was provided by TKI-HTSM 19.0172 and TKI-HTSM 24.0059. R. H. Guis reports was provided by TKI-HTSM 19.0172 and TKI-HTSM 24.0059. Z. Zhou reports a relationship with ASML Netherlands BV that includes: employment. M. U. Arabul reports a relationship with ASML Netherlands BV that includes: employment. If there are other authors, they declare that they have no known competing financial interests or personal relationships that could have appeared to influence the work reported in this paper.

Acknowledgments

R.G., G.J.V. acknowledge support from the project TKI-HTSM/19.0172 and TKI-HTSM/24.0059. The authors gratefully acknowledge Dr. M. Robin for valuable discussions and proofreading the manuscript.

Data availability

Data will be made available on request.

References

[1] A. Kumar, W. Arnold, High resolution in non-destructive testing: a review, J. Appl. Phys. 132 (10) (2022) 100901. https://doi.org/10.1063/5.0095328
[2] H.J. Sharahi, M. Janmaleki, L. Tetard, S. Kim, H. Sadeghian, G.J. Verbiest, Acoustic subsurface-atomic force microscopy: three-dimensional imaging at the nanoscale, J. Appl. Phys. 129 (3) (2021) 030901. https://doi.org/10.1063/5.0035151
[3] A. Briggs, O. Kolosov, Acoustic Microscopy, Monographs on the Physics and Chemistry of Materials, Oxford University Press, Oxford, UK, 2nd edition edition, 2009.
[4] K. Kimura, K. Kobayashi, K. Matsushige, H. Yamada, Imaging of au nanoparticles deeply buried in polymer matrix by various atomic force microscopy techniques, Ultramicroscopy 133 (2013) 41–49. https://doi.org/10.1016/j.ultramic.2013.04.003
[5] P.L.V. Neer, B. Quesson, M.H.V. Es, M.V. Riel, K. Hatakeyama, A. Mohtashami, D. Piras, T. Duivenoorde, M. Lans, H. Sadeghian, Optimization of acoustic coupling for bottom actuated scattering based subsurface scanning probe microscopy, Rev. Sci. Instrum. 90 (7) (2019) 073705. https://doi.org/10.1063/1.5097387
[6] G.J. Verbiest, T.H. Oosterkamp, M.J. Rost, Subsurface contrast due to friction in heterodyne force microscopy, Nanotechnology 28 (8) (2017) 085704. https://doi.org/10.1088/1361-6528/aa53f2
[7] F. Pérez-Cota, R. Fuentes-Domínguez, S.L. Cavera, W. Hardiman, M. Yao, K. Setchfield, E. Moradi, S. Naznin, A. Wright, K.F. Webb, A. Huett, C. Friel, V. Sottile, H.M. Elsheikha, R.J. Smith, M. Clark, Picosecond ultrasonics for elasticity-based imaging and characterization of biological cells, J. Appl. Phys. 128 (16) (2020) 160902. https://doi.org/10.1063/5.0023744
[8] P.A. Elzinga, F.E. Lytle, Y. Jian, G.B. King, N.M. Laurendeau, Pump/Probe spectroscopy by asynchronous optical sampling, Appl. Spectrosc. 41 (1) (1987) 2–4. https://doi.org/10.1366/0003702874868025
[9] A. Bartels, R. Cerna, C. Kistner, A. Thoma, F. Hudert, C. Janke, T. Dekorsy, Ultrafast time-domain spectroscopy based on high-speed asynchronous optical sampling, Rev. Sci. Instrum. 78 (3) (2007) 1–8. https://doi.org/10.1063/1.2714048
[10] J. Bryner, J. Vollmann, L. Aebi, J. Dual, Wave propagation in pyramidal tip-like structures with cubic material properties, Wave Motion 47 (1) (2010) 33–44. https://doi.org/10.1016/j.wavemoti.2009.07.003
[11] D.M. Profunser, J. Vollmann, J. Dual, Ultrasonic wave propagation in focussing tips with arbitrary geometries, Ultrasonics 40 (1–8) (2002) 747–752. https://doi.org/10.1016/S0041-624X(02)00205-6
[12] J. Bryner, Applications of GHz Ultrasound: Material Characterization and Wave Propagation in Microstructures, Ph.D. thesis, ETH, 2009.
[13] R. Delalande, D. Garcia-Sanchez, L. Belliard, Towards acoustic microscopy at the nanoscale by coupling atomic force microscopy with picosecond ultrasonics, Phys. Rev. B 107 (8) (2023) 085409. https://doi.org/10.1103/PhysRevB.107.085409
[14] NuNano, Scout 70, 2024. https://www.nunano.com/store/scout-70.
[15] O. Matsuda, M.C. Larciprete, R.L. Voti, O.B. Wright, Fundamentals of picosecond laser ultrasonics, Ultrasonics 56 (2015) 3–20. https://doi.org/10.1016/j.ultras.2014.06.005
[16] N. Chigarev, C. Rossignol, B. Audoin, Surface displacement measured by beam distortion detection technique: application to picosecond ultrasonics, Rev. Sci. Instrum. 77 (11) (2006) 114901. https://doi.org/10.1063/1.2372739
[17] Femto Datasheet high-speed balanced photoreceiver datasheet HBPR-200M-30K-SI-FST high-speed balanced photoreceiver, 2024. https://www.femto.de/images/pdf-dokumente/de-hbpr-200m-30k-si-fs-fst.pdf. Femto.
[18] Zurich Instruments, UHFLI 600MHz specifications, 2024. https://www.zhinst.com/ch/en/products/uhfli-lock-in-amplifier#specifications.
[19] K. Nakagawa, G. Hashiguchi, H. Kawakatsu, Small single-crystal silicon cantilevers formed by crystal facets for atomic force microscopy, Rev. Sci. Instrum. 80 (095104) (2009). https://doi.org/10.1063/1.3202322
[20] NanoAndMore, AFM Probe Fabrication, 2026. https://www.nanoandmore.com/afm-probe-fabrication.
[21] M. Lee, M.P. Robin, R.H. Guis, U. Filippozzi, D.H. Shin, T.C.V. Thiel, S.P. Paardekooper, J.R. Renshof, H.S. V.D. Zant, A.D. Caviglia, G.J. Verbiest, P.G. Steeneken, Self-sealing complex oxide resonators, Nano Lett. 22 (4) (2022) 1475–1482. arXiv:2109.03978, https://doi.org/10.1021/acs.nanolett.1c03498
[22] P. Ruello, V.E. Gusev, Physical mechanisms of coherent acoustic phonons generation by ultrafast laser action, Ultrasonics 56 (2015) 21–35. https://doi.org/10.1016/j.ultras.2014.06.004
[23] D.G. Cahill, W.K. Ford, K.E. Goodson, G.D. Mahan, A. Majumdar, H.J. Maris, R. Merlin, S.R. Phillpot, Nanoscale thermal transport, J. Appl. Phys. 93 (2) (2003) 793–818. https://doi.org/10.1063/1.1524305
[24] A.A. Barinov, B. Liu, V.I. Khvesyuk, A new technique for modelling phonon scattering processes at rough interfaces and free boundaries of solids, J. Phys.: Conf. Ser. 2150 (1) (2022) 012021. https://doi.org/10.1088/1742-6596/2150/1/012021
[25] A.J. Minnich, J.A. Johnson, A.J. Schmidt, K. Esfarjani, M.S. Dresselhaus, K.A. Nelson, G. Chen, Thermal conductivity spectroscopy technique to measure phonon mean free paths, Phys. Rev. Lett. 107 (9) (2011) 095901. https://doi.org/10.1103/PhysRevLett.107.095901
[26] B.C. Daly, K. Kang, Y. Wang, D.G. Cahill, Picosecond ultrasonic measurements of attenuation of longitudinal acoustic phonons in silicon, Phys. Rev. B - Condens. Matter Mater. Phys. 80 (17) (2009) 174112. https://doi.org/10.1103/PhysRevB.80.174112
[27] H. Liu, M. Lee, M. Šiškins, H.S. V.D. Zant, P.G. Steeneken, G.J. Verbiest, Tuning heat transport in graphene by tension, Phys. Rev. B 108 (8) (2023) L081401. https://doi.org/10.1103/PhysRevB.108.L081401
[28] M.A. Hopcroft, W.D. Nix, T.W. Kenny, What is the Young's modulus of silicon?, J. Microelectromech. Syst. 19 (2) (2010) 229–238. https://doi.org/10.1109/JMEMS.2009.2039697

[29] F.H. Quintanilla, M.J.S. Lowe, R.V. Craster, Modeling guided elastic waves in generally anisotropic media using a spectral collocation method, J. Acoust. Soc. Am 137 (2015) 1180–1194. https://doi.org/10.1121/1.4913777
[30] M. Robin, R. Guis, M.U. Arabul, Z. Zhou, N. Pandey, G.J. Verbiest, Experimental and numerical study of conoscopic interferometry sensitivity for optimal acoustic pulse detection in ultrafast acoustics, Photoacoustics 30 (2023) 100470. https://doi.org/10.1016/j.pacs.2023.100470
[31] M.S. Kim, W.R. Lee, Y.Y. Kim, J.H. Oh, Transmodal elastic metasurface for broad angle total mode conversion, Appl. Phys. Lett. 112 (2018) 261902. https://doi.org/10.1063/1.5032157
[32] R.J. Dolleman, Y.M. Blanter, H.S. V.D. Zant, P.G. Steeneken, G.J. Verbiest, Phonon scattering at kinks in suspended graphene, Phys. Rev. B 101 (2020) 115411. https://doi.org/10.1103/PhysRevB.101.115411
[33] A.G. Webster, Acoustical impedance and the theory of horns and of the phonograph, Proc. Natl. Acad. Sci. U. S. A. 5 (7) (1919) 275–282. https://doi.org/10.1073/pnas.5.7.275
[34] S. Sherrit, X. Bao, Y. Bar-Cohen, Solid micro horn array (SMIHA) for acoustic matching, in: Proceedings of SPIE: Sensors and Smart Structures Technologies for Civil, Mechanical, and Aerospace Systems 2008, Vol. 6932, SPIE, San Diego, CA, USA, 2008, p. 69322X. https://doi.org/10.1117/12.776384
[35] R.S. Sangam, R.S. Kshetrimayum, Linear tapers: analysis, design and applications, in: IEEE MTT-S International Microwave and RF Conference (IMaRC), IEEE, Kolkata, India, 2018, pp. 1–4. https://doi.org/10.1109/IMaRC.2018.8877280
[36] P. Choochalerm, W.E. Martin, H.R. Jones, R. Errmann, S. Yerolatsitis, T.A. Wright, C. Buisset, Transmission properties of tapered optical fibres: simulations and experimental measurements, Opt. Fiber Technol. 66 (2021) 102632. https://doi.org/10.1016/j.yofte.2021.102632
[37] D.M. Pozar, Microwave Engineering, John Wiley & Sons, Hoboken, NJ, USA, 4th edition edition, 2011.